maps. In FDG-PET, the data of the normal elderly template in our institute ($n = 41$, 51–78 years) were used as a reference for the patients with Alzheimer's disease. The data of the normal volunteers whose age and eligibility were matched with this protocol were used in normal elderly template. Thresholds of $P < 0.005$ and $P < 0.01$ corrected for the cluster level were applied to [^{11}C]MPDX and FDG-PET images, respectively. The clusters with an extent of greater than 300 voxels were considered. For visualization of the t score statistics [SPM (t) map], the significant voxels were projected onto the 3D rendered brain of a standard high-resolution MRI template provided by SPM2, thus allowing anatomical identification.

Results

In the ROI-based analysis, the binding potential of [^{11}C]MPDX in normal elderly subjects was high in the striatum and thalamus and low in the cerebellum and pons. The binding potential of [^{11}C]MPDX in patients with Alzheimer's disease was high in the striatum and thalamus and low in the medial temporal cortex and cerebellum. The binding potential of [^{11}C]MPDX in patients with Alzheimer's disease was significantly lower in the temporal, medial temporal cortices, and thalamus than that in normal elderly subjects ($P = 0.038$, 0.028, and 0.039, respectively; Fig. 2). Especially, the binding potential of [^{11}C]MPDX in the medial temporal cortex in patients with Alzheimer's disease was nearly equal to that in the cerebellum.
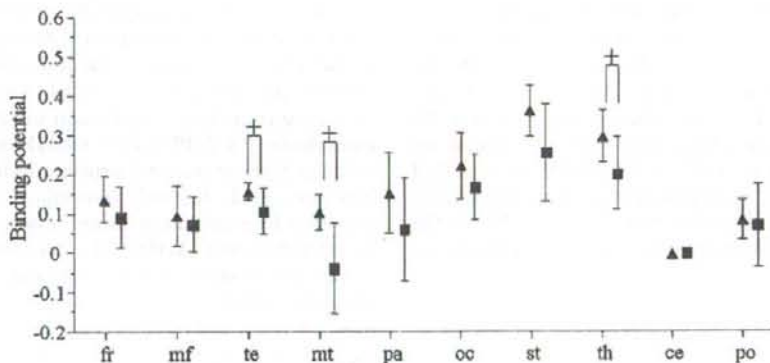
The SPM analysis of [^{11}C]MPDX PET between patients with Alzheimer's disease and normal elderly subjects is shown in Fig. 3a. The binding potential was widely and severely decreased in the temporal, medial temporal cortices, and thalamus, and partially decreased in the parietal cortex in patients with Alzheimer's disease with significance ($P < 0.005$, corrected $k > 300$). Decreased binding potential was slightly prominent in the left hemisphere.

The SPM analysis of FDG-PET in the same patients with Alzheimer's disease is shown in Fig. 3b. The FDG uptake was widely and severely decreased in the temporoparietal cortex and posterior cingulate gyrus with significance ($P < 0.01$, corrected $k > 300$). Decreased FDG uptake was slightly prominent in the left hemisphere.

Discussion

In Alzheimer's disease subjects, ROI-based analysis and SPM analysis clearly demonstrated the decreased binding potential of [^{11}C]MPDX in the temporal and medial temporal cortices and thalamus when compared with normal elderly subjects as shown in Figs. 2 and 3a. The finding of decreased binding potential in the medial temporal cortex is consistent with past postmortem autoradiographic and pathological studies of patients with Alzheimer's disease [19–22]. Ulas et al. [20] reported that decreased A_1 agonist binding was observed in the CA1 stratum oriens and outer layers of the parahippocampal gyrus, whereas decreased antagonist binding was found in the subiculum and CA3 region. Adenosine A_1 recep-

Fig. 2 Binding potential of [^{11}C]MPDX in the human brain. Patients with Alzheimer's disease showed a significantly lower value in the temporal and medial temporal cortices and thalamus than normal elderly volunteers. The value in the cerebellum was zero because the value was calculated based on the assumption that adenosine A_1 receptors are very sparse in the cerebellum. Abbreviations used are the same as in Fig. 1. *Triangle* normal elderly subjects ($n = 8$), *square* patients with Alzheimer's disease ($n = 6$), *plus* $P < 0.05$ compared between normal elderly subjects and patients with Alzheimer's disease
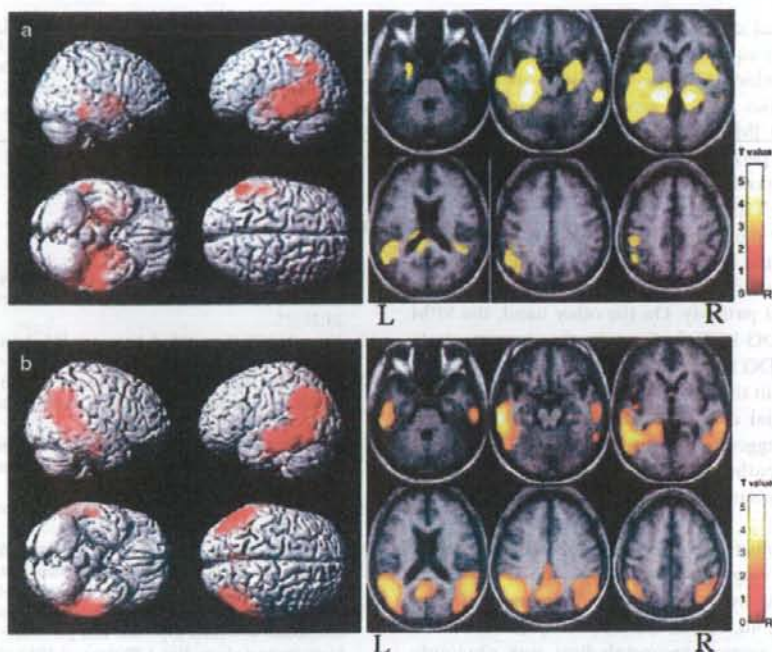
Fig. 3 Statistical analyses of the binding potential of [¹¹C]MPDX (a) and standardized uptake value (SUV) of [¹⁸F]fluorodeoxyglucose (FDG, **b**) in patients with Alzheimer's disease. *Left* Statistical parametric mapping (SPM) Z maps are superimposed onto the right lateral, left lateral, inferior, and superior views (from *left upper* to *right lower*) of a volume-rendered spatially normalized magnetic resonance imaging (MRI) study. *Right* SPM Z maps are superimposed onto the axial views of a spatially normalized T1-MRI study. Each image represents from the *bottom* (*left upper*) to the *top* (*right lower*). *Red* and *yellow* represent the areas with significant reduction in binding potential or SUV. **a** Decreased binding potential of [¹¹C]MPDX was noted in the temporal, medial temporal cortices, and thalamus widely and parietal cortex partially. Decreased binding is slightly prominent in the left hemisphere. **b** Decreased SUV of FDG was noted in the temporo-parietal cortices. Decreased SUV is slightly prominent in the left hemisphere

tors are located on the terminal of the perforant pathway which provides a major input to the molecular layer of the dentate gyrus [34]. It has been reported that the perforant pathway contributes 80%–85% of the synapses on the outer portion of the dendrites that arise from the dentate gyrus granule cells [34, 35]. The cells of origin of the perforant pathway in the entorhinal cortex are destroyed in the brain of patients with Alzheimer's disease [34]. Decreased binding potential of [¹¹C]MPDX in the medial temporal cortex is considered to be affected by insufficiency or damage to the perforant pathway in patients with Alzheimer's disease. Decreased binding potential of [¹¹C]MPDX in the temporal cortex in patients with Alzheimer's disease can be directly or indirectly correlated with destruction of the cells of origin of the perforant pathway. Thalamic nuclei have strong reciprocal connections with the cerebral cortex, forming thalamo-cortico-thalamic circuits. An abnormal finding

in the thalamus of Alzheimer's disease has been described in a few MRI reports [36, 37]. It is considered that decreased binding potential of [¹¹C]MPDX in the thalamus is derived from corticothalamic transmission from the temporal and medial temporal cortices. The reason for the laterality in [¹¹C]MPDX and FDG-PET can be derived from investigations of small numbers ($n = 6$) of patients. Laterality in FDG-PET was also reported in a study with a small number of patients with Alzheimer's disease [38]. It is necessary to investigate these issues in greater number of patients.

We calculated the binding potential as a reference for the cerebellar cortex because the cerebellar cortex showed very low adenosine A₁ receptor densities [39] and this method provided well-balanced data in our earlier study [28]. The calculated binding potential of [¹¹C]MPDX in the medial temporal cortex was slightly lower than 0, which means that adenosine A₁ receptor density in the

medial temporal cortex in patients with Alzheimer's disease is nearly equal to or lower than that in the cerebellar cortex which contains very low adenosine A_1 receptor densities [39]. A severely decreased binding potential of [^{11}C]MPDX in the medial temporal cortex means that the perforant pathway in the medial temporal cortex is markedly insufficient or damaged in patients with Alzheimer's disease.

We consider that the decreased binding potential of [^{11}C]MPDX in the temporal and medial temporal cortices directly or indirectly reflects insufficiency or damage to the perforant pathway. On the other hand, the SPM analysis of FDG-PET findings in the present study revealed that FDG uptake was decreased in the temporal cortex and not in the medial temporal cortex, where the binding potential of [^{11}C]MPDX decreased markedly. The findings suggested that insufficiency or damage to the perforant pathway in the medial temporal cortex could not necessarily be reflected by the FDG-PET results.

Hypometabolism in the temporo-parietal cortex and posterior cingulate gyrus (Fig. 3b) is a typical pattern revealed by FDG-PET in Alzheimer's disease subjects [23–25, 40, 41]. In the temporo-parietal cortex, the area with severe hypometabolism was obviously larger than that with decreased binding potential of [^{11}C]MPDX in patients with Alzheimer's disease. In the posterior cingulate gyrus, [^{11}C]MPDX PET was not coupled with hypometabolism. Therefore, FDG-PET is more sensitive in detecting the degeneration of the temporo-parietal cortex and posterior cingulate gyrus, which is a typical manifestation in Alzheimer's disease, than [^{11}C]MPDX PET. However, it is well known that FDG-PET in Alzheimer's disease does not necessary reflect the pathological changes [42–44]. [^{11}C]MPDX PET provides a different diagnostic tool than FDG-PET, and could be valuable in detecting the degeneration in the medial temporal cortex. In addition, [^{11}C]MPDX PET has the possibility to detect corticothalamic transmission from the temporal and medial temporal cortices.

Conclusions

In patients with Alzheimer's disease, the binding potential of [^{11}C]MPDX decreased significantly in the temporal and medial temporal cortices and thalamus, and a small or no decrease was observed in the parietal cortex and posterior cingulate gyrus. The pattern of the binding potential of [^{11}C]MPDX had the possibility to be different from that of the FDG-PET in patients with Alzheimer's disease.

References

1. Dunwiddie TV, Masino SA. The role and regulation of adenosine in the central nervous system. Ann Rev Neurosci 2001; 24:31–55.
2. Yacoubi ME, Costentin J, Vaugeois JM. Adenosine A_{2A} receptors and depression. Neurology 2003;61:S82–7.
3. von Lubitz DK. Adenosine in the treatment of stroke: yes, maybe, or absolutely not? Expert Opin Investig Drugs 2001; 10:619–32.
4. Haas HL, Selbach O. Functions of neuronal adenosine receptors. Naunyn Schmiedebergs Arch Pharmacol 2000;362: 375–81.
5. Collis MG, Hourani SMO. Adenosine receptor subtypes. Trends Pharmacol Sci 1993;14:360–6.
6. Fredholm BB, Abbracchio MP, Burnstock G, Daly JW, Harden TK, Jacobson KA, et al. Nomenclature and classification of purinoceptors. Pharmacol Rev 1994;46:143–56.
7. Corradetti R, Lo Conte G, Moroni F, Passani MB, Pepeu G. Adenosine decreases aspartate and glutamate release from rat hippocampal slices. Eur J Pharmacol 1984;104:19–26.
8. Dolphin AC, Archer ER. An adenosine agonist inhibits and a cyclic AMP analogue enhances the release of glutamate but not GABA from slices of rat dentate gyrus. Neurosci Lett 1983;43:49–54.
9. Dunwiddie TV. The physiological role of adenosine in the central nervous system. Int Rev Neurobiol 1985;27:63–139.
10. Fredholm BB, Dunwiddie TV. How does adenosine inhibit transmitter release? Trends Pharmacol Sci 1988;9:130–4.
11. Fredholm BB, Hedqvist P. Modulation of neurotransmission by purine nucleotides and nucleosides. Biochem Pharmacol 1980;29:1635–43.
12. Phillis JW, Wu PH. The role of adenosine and its nucleotides in central synaptic transmission. Prog Neurobiol 1981;16: 187–239.
13. Schoenberg BS. Epidemiology of Alzheimer's disease and other dementing disorders. J Chronic Dis 1986;39:1095–104.
14. Fratiglioni L, Grut M, Forsell Y, Viitanen M, Grafstrom M, Holmen K, et al. Prevalence of Alzheimer's disease and other dementias in an elderly urban population: relationship with age, sex, and education. Neurology 1991;41:1886–92.
15. Brookmeyer R, Gray S, Kawas C. Projections of Alzheimer's disease in the United States and the public health impact of delaying disease onset. Am J Public Health 1998;88:1337–42.
16. Weinberger M, Gold DT, Divine GW, Cowper PA, Hodgson LG, Schreiner PJ, et al. Expenditures in caring for patients with dementia who live at home. Am J Public Health 1993; 83:338–41.
17. Osttbye T, Crosse E. Net economic costs of dementia in Canada. CMAJ 1994;151:1457–63.
18. Ernst R, Hay JW, Fenn C, Tinklenberg J, Yesavage JA. Cognitive function and the costs of Alzheimer's disease. Arch Neurol 1997;54:687–93.
19. Jansen K, Faull RLM, Dragunow M, Synek BJL. Alzheimer's disease: changes in hippocampal N-methyl-D-aspartate, quisqualate, neurotensin, adenosine, benzodiazepine, sero-

tonin and opioid receptors: an autoradiographic study. Neuroscience 1990;39:613–27.

20. Ulas J, Brunner LC, Nguyen L, Cotman CW. Reduced density of adenosine A1 receptors and preserved coupling of adenosine A1 receptors to G proteins in Alzheimer hippocampus: a quantitative autoradiographic study. Neuroscience 1993;52:843–54.

21. Jaarsma D, Sebens B, Korf J. Reduction of adenosine A1-receptors in the perforant pathway terminal zone in Alzheimer hippocampus. Neurosci Lett 1991;121:111–4.

22. Kalaria RN, Sromek S, Wilcox BJ, Unnerstall JR. Hippocampal adenosine A1 receptors are decreased in Alzheimer's disease. Neurosci Lett 1990;118:257–60.

23. Ishii K, Sasaki H, Kono AK, Miyamoto N, Fukuda T, Mori E. Comparison of gray matter and metabolic reduction in mild Alzheimer's disease using FDG-PET and voxel-based morphometric MR studies. Eur J Nucl Med 2005;32:959–63.

24. Mosconi L. Brain glucose metabolism in the early and specific diagnosis of Alzheimer's disease. FDG-PET studies in MCI and AD. Eur J Nucl Med 2005;32:486–510.

25. Meguro K, LeMestric C, Landeau B, Desgranges B, Eustache F, Baron JC. Relations between hypometabolism in the posterior association neocortex and hippocampal atrophy in Alzheimer's disease: a PET/MRI correlative study. J Neurol Neurosurg Psychiatry 2001;71:315–21.

26. Fukumitsu N, Ishii K, Kimura Y, Oda K, Sasaki T, Mori Y, et al. Imaging of adenosine A_1 receptors in the human brain by positron emission tomography with [^{11}C]MPDX. Ann Nucl Med 2003;17:511–5.

27. Fukumitsu N, Ishii K, Kimura Y, Oda K, Sasaki T, Mori Y, et al. Adenosine A_1 receptor mapping of the human brain by PET with 8-dicyclopropylmethyl-1-11C-methyl-3-propylxanthine. J Nucl Med 2005;46:32–7.

28. Kimura Y, Ishii K, Fukumitsu N, Oda K, Sasaki T, Kawamura K, et al. Quantitative analysis of adenosine A_1 receptors in human brain using positron emission tomography and [1-methyl-^{11}C]8-dicyclopropylmethyl-1-methyl-3-propylxanthine. Nucl Med Biol 2004;31:975–81.

29. Naganawa M, Kimura Y, Nariai T, Ishii K, Oda K, Manabe Y, et al. Omission of serial arterial blood sampling in neuroreceptor imaging with independent component analysis. Neuroimage 2005;26:885–90.

30. Zigmond AS, Snaith RP. The Hospital Anxiety and Depression Scale. Acta Psychiatr Scand 1983;67:361–7.

31. Noguchi J, Ishiwata K, Furuta R, Simada J, Kiyosawa M, Ishii S, et al. Evaluation of carbon-11 labeled KF15372 and its ethyl and methyl derivatives as a potential CNS adenosine A_1 receptor ligand. Nucl Med Biol 1997;24:53–9.

32. Ishiwata K, Nariai T, Kimura Y, Oda K, Kawamura K, Ishii K, et al. Preclinical studies on [^{11}C]MPDX for mapping adenosine A_1 receptors by positron emission tomography. Ann Nucl Med 2002;16:377–82.

33. Ardekani BA, Braun M, Hutton BF, Kanno I, Iida H. A fully automatic multimodality image registration algorithm. J Comput Assist Tomog 1995;19:615–23.

34. Dragunow M, Murphy K, Leslie RA, Robertson HA. Localization of adenosine A1-receptors to the terminals of the perforant path. Brain Res 1988;462:252–7.

35. Hyman BT, Van Hoesen GW, Kromer LJ, Damasio AR. Perforant pathway changes and the memory impairment of Alzheimer's disease. Ann Neurol 1986;20:472–81.

36. Stephen RE, Janke AL, Chark JB. Gray and white matter changes in Alzheimer's disease: a diffusion tensor imaging study. J Magn Reson Imaging 2008;27:20–6.

37. Medina D, DeToledo-Morrell L, Urresta F, Gabrieli JD, Moseley M, Fleischman D, et al. White matter changes in mild cognitive impairment and AD: a diffusion tensor imaging study. Neurobiol Aging 2006;27:663–72.

38. Zahn R, Juengling F, Bubrowski P, Jost E, Dykierek P, Talazko J, et al. Hemisphere asymmetries of hypometabolism associated with semantic memory impairment in Alzheimer's disease: a study using positron emission tomography with fluorodeoxyglucose-F18. Psychiatry Res Neuroimaging 2004;132:159–72.

39. Fastbom J, Pazos A, Probst A, Palacios JM. Adenosine A1 receptors in the human brain: a quantitative autoradiographic study. Neuroscience 1987;22:827–39.

40. Sakamoto S, Ishii K, Sasaki M, Hosaka M, Mori T, Matsui M, et al. Differences in cerebral metabolic impairment between early and late onset types of Alzheimer's disease. J Neurol Sci 2002;15:27–32.

41. Kim EJ, Cho SS, Jeong Y, Park KC, Kang E, Kim SE, et al. Glucose metabolism in early onset versus late onset Alzheimer's disease: an SPM analysis of 120 patients. Brain 2005;128:1790–801.

42. Ibanez V, Pietrini P, Alexander GE, Furey ML, Teichberg D, Rajapakse JC, et al. Regional glucose metabolic abnormalities are not the result of atrophy in Alzheimer's disease. Neurology 1998;50:1585–93.

43. Mosconi L, Sorbi S, de Leon MJ, Li Y, Nacmias B, Myoung PS, et al. Hypometabolism exceeds atrophy in presymptomatic early-onset familial Alzheimer's disease. J Nucl Med 2006;47:1778–86.

44. Chetelat G, Desgranges B, Landeau B, Mezenge F, Poline JB, de la Sayette V, et al. Direct voxel-based comparison between grey matter hypometabolism and atrophy in Alzheimer's disease. Brain 2008;131:60–71.

ORIGINAL ARTICLE

Low density of sigma₁ receptors in early Alzheimer's disease

**Masahiro Mishina · Masashi Ohyama · Kenji Ishii
Shin Kitamura · Yuichi Kimura · Kei-ichi Oda
Kazunori Kawamura · Toru Sasaki · Shiro Kobayashi
Yasuo Katayama · Kiichi Ishiwata**

Abstract

Objective The sigma₁ receptor is considered to be
involved in cognitive function. A postmortem study
reported that the sigma₁ receptors were reduced in the
hippocampus in Alzheimer's disease (AD). However, in
vivo imaging of sigma₁ receptors in the brain of AD
patients has not been reported. The aim of this study is
to investigate the mapping of sigma₁ receptors in AD
using [^{11}C]SA4503 positron emission tomography
(PET).

M. Mishina · M. Ohyama · K. Ishii · Y. Kimura · K. Oda ·
K. Kawamura · T. Sasaki · K. Ishiwata
Positron Medical Center, Tokyo Metropolitan Institute of
Gerontology, Tokyo, Japan

M. Mishina · M. Ohyama · S. Kitamura · Y. Katayama
Department of Neurology, Nephrology and Rheumatology,
Nippon Medical School, Tokyo, Japan

M. Mishina (✉) · S. Kobayashi
Neurological Institute, Nippon Medical School Chiba-Hokusoh
Hospital, 1715 Kamagari, Imba-mura, Imba-gun, Chiba 270-
1694, Japan
e-mail: mishina@nms.ac.jp

S. Kitamura
Department of Internal Medicine, Nippon Medical School
Musashi Kosugi Hospital, Kanagawa, Japan

Y. Kimura
Biophysics Group, Molecular Imaging Center, National Institute
of Radiological Sciences, Chiba, Japan

K. Kawamura
Center for Integrated Brain Science, Brain Research Institute,
University of Niigata, Niigata, Japan

T. Sasaki
Research Team for Molecular Biomarkers, Tokyo Metropolitan
Institute of Gerontology, Tokyo, Japan

Methods We studied five AD patients and seven elderly
volunteers. A dynamic series of decay-corrected PET
data acquisition was performed for 90 min starting at the
time of the injection of 500 MBq of [^{11}C]SA4503. A two-
tissue three-compartment model was used to estimate
K_1, k_2, k_3, k_4, and the delay between metabolite-corrected
plasma and tissue time activity using a Gauss–Newton
algorithm. The ratio of k_3 to k_4 was computed as the
binding potential (BP), which is linearly related to the
density of sigma₁ receptors. Unpaired t tests were used
to compare K_1 and BP in patients with AD and normal
subjects.
Results As compared with normals, BP in the AD was
significantly lower in the frontal, temporal, and occipital
lobe, cerebellum and thalamus, whereas K_1 was signifi-
cantly lower in the parietal lobe.
Conclusions [^{11}C]SA4503 PET can demonstrate that the
density of cerebral and cerebellar sigma₁ receptors is
reduced in early AD.

Introduction

Sigma₁ receptor has received considerable attention in
the regulation of cognitive function [1]. The sigma
receptor has been established as a distinct receptor,
although it was initially proposed as a subtype of opioid
receptors [2]. It is classified into at least two subtypes,
namely, sigma₁ and sigma₂ [3]. Although an endogenous
ligand for the sigma receptors remains unclear, some
studies have reported that steroid hormones such as
progesterone and testosterone might interact with sigma

receptors [4, 5]. Confirmed sigma$_1$ receptor ligand functions are neuro-protective, anti-depressant, and anti-amnestic functions [6, 7]. Sigma$_1$ receptor agonists improved impairment of learning and memory in mice [8–10]. Matsuno et al. [11–13] showed that the sigma$_1$ receptor agonists such as (+)-SKF-10,047 and SA4503 increased extracellular acetylcholine levels in the rat frontal cortex and hippocampus. The sigma$_1$ receptor is considered to be involved in aging [14, 15] and various diseases, such as schizophrenia [16], depression [17], ischemia [18], and Parkinson's disease [19]. In patients with Alzheimer's disease (AD), a postmortem study showed that the sigma$_1$ binding sites were reduced in the hippocampus [20]. The sigma$_1$ receptor agonists are also expected as drugs for improving the cognitive deficits of AD [21]. However, the distribution of sigma$_1$ receptors in patients with AD remains to be determined. We developed a positron emission tomography (PET) ligand, [^{11}C]SA4503 (Fig. 1), for mapping the sigma$_1$ receptors [22–24], and reported that sigma$_1$ receptor was down-regulated in the putamen with Parkinson's disease [19]. The objective of this study was to investigate the change of sigma$_1$ receptor in the early phase of AD using [^{11}C]SA4503 PET.

Materials and methods

Subjects

We studied five patients (two men and three women, mean age ± SD, 74.6 ± 3.2 years) diagnosed as having probable AD on the basis of the National Institute of Neurological and Communicative Diseases and Stroke/ Alzheimer's Disease and Related Disorders Association (NINCDS–ADRDA) criteria [25]. Magnetic resonance imaging (MRI) scans were obtained with a MAGNEX 1.5-T machine (Shimadzu, Kyoto, Japan) in the First Hospital of Nippon Medical School, and we confirmed that they had no diseases other than AD including stroke and brain tumor. To ensure the early diagnosis of AD, each patient was also examined for glucose metabolism by PET using [^{18}F]fluorodeoxyglucose ([^{18}F]FDG), and
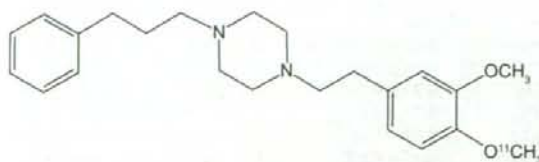
we confirmed hypometabolism of glucose in the temporoparietal lobe and posterior cingulate of all patients [26, 27]. The clinical severity of AD was scored in each patient according to the Functional Assessment of Staging [28], Mini-Mental State examination [29], and Clinical Dementia Rating [30] just before the [^{18}F]FDG PET examination.

The control group consisted of seven volunteers (two men and four women, age ± SD 62.6 ± 8.2), without any history of neurological diseases or abnormalities on physical or neurological examinations. MRI scans were obtained with a SIGNA 1.5-T machine (General Electric, WI, USA) in the Tokyo Metropolitan Geriatric Hospital for the normal subjects, and we confirmed that they had no neurological diseases, such as stroke and brain tumor. They were not currently receiving medications known to affect brain metabolism. None had a history of alcoholism.

The Ethics Committee of Tokyo Metropolitan Institute of Gerontology approved this study protocol. Informed consent in writing was obtained from all of the subjects who participated in this study.

[^{11}C]SA4503 PET

Positron emission tomography was performed in the Tokyo Metropolitan Institute of Gerontology Positron Medical Center with an SET2400 W scanner (Shimadzu, Kyoto, Japan) [31]. [^{11}C]SA4503 was prepared as described earlier [23]. The specific activity at the time of injection ranged from 23.7 GBq/μmol to 130.2 GBq/ μmol (72.3 ± 34.3 GBq/μmol). The transmission data were acquired with a rotating ^{68}Ga/^{68}Ge rod source for attenuation correction. A dynamic series of decay-corrected PET data acquisition was performed in the 2D mode for 90 min starting at the time of the injection of 500 MBq of [^{11}C]SA4503. Arterial blood was sampled at 10 s, 20 s, 30 s, 40 s, 50 s, 60 s, 70 s, 80 s, 90 s, 100 s, 110 s, 120 s, 135 s, and 150 s, and at 3 min, 5 min, 7 min, 10 min, 15 min, 20 min, 30 min, 40 min, 50 min, 60 min, 75 min, and 90 min. Plasma was separated, weighed, and measured for radioactivity with an NaI (Tl) well scintillation counter. Metabolite analysis was carried out by high-performance liquid chromatography [23].

Data analysis

Image manipulations were carried out on an O2 workstation (Silicon Graphics, Mountain View, CA, USA), using a medical image processing application package "Dr. View" version 5.2 (AJS, Tokyo, Japan).

Fig. 1 Chemical structure of [^{11}C]SA4503

For [^{11}C]SA4503 PET, we generated early images for each subject by adding up the frames of the dynamic scan from 0 min to 10 min [32]. Circular regions of interest (ROIs) 10 mm in diameter and extending over two slices of the images were drawn on the cerebellum, medial temporal lobe (included hippocampus), frontal lobe, temporal lobe, occipital lobe, parietal lobe, post cingulate gyrus, thalamus, and striatum. The time course of the tissue concentration of [^{11}C]SA4503 was computed from the PET data and the interpolated ROIs throughout the scanning period. A two-tissue three-compartment model was used to estimate K_1, k_2, k_3, k_4, and the delay between metabolite-corrected plasma and tissue time activity using a Gauss–Newton algorithm [15]. The ratio of k_3 to k_4 was computed as the binding potential (BP), which is linearly related to the density of sigma$_1$ receptors. Parametric images of total distribution volume (DVt) for [^{11}C]SA4503 were also generated using a graphical analysis [33].

Statistics

Unpaired t tests were used to compare the BP in patients with AD and normal subjects. The Bonferroni correction was applied for multiple comparisons (nine comparisons corresponding to nine regions). The level of significance was set at $P < 0.05$. The statistical computation was performed using a software package "JMP" version 5.1.2 (SAS Institute, Cary, NC, USA) on a Macintosh computer.

Results

Table 1 summarizes the clinical profiles. Their average duration of illness was 2.0 ± 0.7 years. The severity of cognitive dysfunction as assessed with the Mini-Mental State examination ranged from 16 to 25.

In the ROI-based analysis, K_1 for [^{11}C]SA4503 was significantly lower in the parietal lobe of the AD patients than in that of normals, whereas there was no significant difference in other regions between AD patients and the normals (Table 2). On the other hand, BP for [^{11}C]SA4503 was significantly lower in the frontal, temporal, and occipital lobes, cerebellum and thalamus of the AD patients than in that of normals (Table 2). We also observed that BP also showed a tendency to decline in other regions of AD. Figure 2 shows representative PET images for a normal subject and a patient with AD. The DVt image demonstrates that the sigma$_1$ receptors are lower in the entire brain of the patient with AD than in that of the normal subject.

Discussion

[^{11}C]SA4503 PET demonstrated that the distribution of cortical sigma$_1$ receptors was reduced in the early phase of AD. Only in the parietal lobe could we observe a significant reduction of K_1, which was linearly related to the cerebral blood flow. The age of the control subjects was slightly younger than that of the patient group. However,

Table 1 Demographic and clinical data for patients with Alzheimer's disease (AD)

No.	Age (years)	Sex	Duration (year)	Medication before PET	FAST	MMS	CDR
1	79	M	3	Donepezil	3	25	1
2	76	M	2	Donepezil	3	21	1
3	75	F	1	Donepezil	4	16	1
4	71	F	2	None	3	17	1
5	72	F	2	None	3	22	1

PET positron emission tomography, *FAST* functional assessment of staging, *MMS* Mini-Mental State examination, *CDR* clinical dementia rating

Table 2 Comparison of K_1 and binding potential for sigma$_1$ receptors in each region in normals and patients with AD

ROI regions of interest, *BP* binding potential, *AD* Alzheimer's disease Values are mean ± SD (normal $n = 7$, AD $n = 5$). *$P < 0.05$, **$P < 0.01$ (unpaired t test)

ROI	K_1		BP	
	Normal	AD	Normal	AD
Frontal lobe	0.50 ± 0.06	0.43 ± 0.06	16.4 ± 3.0	9.2 ± 4.5*
Temporal lobe	0.52 ± 0.07	0.44 ± 0.04	17.4 ± 3.6	8.7 ± 4.3*
Hippocampus	0.46 ± 0.06	0.42 ± 0.03	18.6 ± 3.8	12.2 ± 6.8
Occipital lobe	0.58 ± 0.07	0.50 ± 0.09	13.7 ± 2.6	5.9 ± 3.3**
Parietal lobe	0.52 ± 0.06	0.39 ± 0.06*	16.7 ± 2.6	13.6 ± 10.5
Posterior cingulate	0.62 ± 0.08	0.50 ± 0.09	15.4 ± 3.2	8.7 ± 5.4
Cerebellum	0.56 ± 0.10	0.58 ± 0.06	22.5 ± 4.8	9.0 ± 5.1**
Striatum	0.55 ± 0.07	0.57 ± 0.07	13.9 ± 2.4	8.8 ± 3.5
Thalamus	0.64 ± 0.09	0.62 ± 0.09	15.2 ± 4.7	6.9 ± 2.3*

Fig. 2 Positron emission tomography (PET) images for a 65-year-old healthy woman (**a**), and a 71-year-old woman with Alzheimer's disease (**b**). Parametric images for the DVt of [^{11}C]SA4503 were generated using a graphical analysis. [^{11}C]SA4503 PET demonstrates that the sigma$_1$ receptors are widely distributed throughout the entire brain in a normal subject (**a**). In comparison with the normal subject, the number of sigma$_1$ receptors was decreased in the brain of the patient with Alzheimer's disease (**b**)

when the BP in the control subjects (62.6 ± 8.2 years) was compared with that in the young subjects ($n = 9$, 28 ± 4 years) reported earlier [24], it was found to be slightly decreased with aging without statistical significance (unpublished data) in spite of an age-dependent increase of the [^{11}C]SA4503 binding in rats and monkeys [14, 15]. The reduction of the BP in AD was much more marked compared with the BP in the aged control subjects. Therefore, the reduced sigma$_1$ receptor density in AD could not be derived from the slight difference in age between the control and patient groups. PET with [^{18}F]FDG and statistical image analysis applications such as statistical parametric mapping (SPM) and 3D stereotactic surface projections have shown that in patients with AD, the cerebral glucose metabolism is reduced in the temporal-, parietal-, posterior cingulate-, and prefrontal regions [26, 27]. We also confirmed a similar pattern in the present patients with AD by [^{18}F]FDG PET (data not shown). However, these findings did not correspond with the distribution of neuronal loss on postmortem studies [34]. In a [^{11}C]flumazenil PET study on AD, Ohyama et al. [35] showed that benzodiazepine receptor was less impaired than neuronal function assessed by the cerebral blood flow and glucose metabolism in the association-cortex. The benzodiazepine receptors are one of the gamma-aminobutyric acid type A (GABA$_A$) receptor complex. The present study indicated that sigma$_1$ receptors were affected from the early stages of AD, unlike GABA$_A$ receptors. Some articles showed that the sigma$_1$ receptor agonists increased extracellular acetylcholine levels in the rat frontal cortex and hippocampus [11, 12]. Increased

acetylcholine does not directly affect the [^{11}C]SA4503 binding, because acetylcholine does not bind to sigma$_1$ receptors. However, reduction of the number of sigma$_1$ receptors may reflect the cholinergic system and cognitive function of patients with AD. Amyloid imaging by PET currently represents a potentially useful tool for the early diagnosis of pre-onset AD [36]. We have an interest in the relationship between sigma$_1$ receptor in the mild cognitive impairment stage and pre-onset stage of AD. Further studies will be needed using amyloid PET and [^{11}C]SA4503 PET.

The density of sigma$_1$ receptors in the cerebellum was significantly lower in AD than in normals, although K_1 in AD was comparable with that in normals. Although the cerebellum was formerly thought to be unaffected in AD, many studies have revealed cerebellar changes in AD patients [37–43]. A pathological study showed that the density of Purkinje cell was reduced in the cerebellum of AD, especially in the vermis [41]. Using glutamate as the neurotransmitter, the granule cells deliver an excitability signal to the dendrite of Purkinje cells. Chaki et al. [44] suggested that sigma$_1$ binding sites are involved in modulating the release of dopamine by interacting with N-methyl-D-aspartic acid (NMDA) receptors on dopaminergic nerve terminals. Release of dopamine is reduced in the putamen with Parkinson's disease, and sigma$_1$ receptors were down-regulated in the putamen with Parkinson's disease [19]. Sigma$_1$ receptors in the cerebellum may be involved in the modulation of glutamate receptor, as well as in the putamen.

Although we could observe a reduced density of sigma$_1$ receptors in the early phase of AD, we cannot say that [^{11}C]SA4503 PET is suitable for the early diagnosis of AD. We are obliged to force the subjects to remain still for over 100 min with their heads fixed in a PET machine and to cannulate their radial artery to sample the arterial blood. Most AD patients are not suitable for the protocol of [^{11}C]SA4503 PET. Prior to the examinations, we had to confirm whether each of the AD subjects in the current study could withstand the protocol of [^{11}C]SA4503 PET. Therefore, we are now investigating a shortened protocol for [^{11}C]SA4503 PET; 40- to 60-min PET scans without arterial blood sampling could possibly provide reliable results in the practical application, which will be described elsewhere.

References

1. Hashimoto K, Ishiwata K. Sigma receptor ligands: possible application as therapeutic drugs and as radiopharmaceuticals. Curr Pharm Des 2006;12:3857–76.

2. Walker JM, Bowen WD, Walker FO, Matsumoto RR, De Costa B, Rice KC. Sigma receptors: biology and function. Pharmacol Rev 1990;42:355–402.

3. Quirion R, Bowen WD, Itzhak Y, Junien JL, Musacchio JM, Rothman RB, et al. A proposal for the classification of sigma binding sites. Trends Pharmacol Sci 1992;13:85–6.

4. Su TP, London ED, Jaffe JH. Steroid binding at sigma receptors suggests a link between endocrine, nervous, and immune systems. Science (New York) 1988;240:219–21.

5. Su TP. Delineating biochemical and functional properties of sigma receptors: emerging concepts. Critical Rev Neurobiol 1993;7:187–203.

6. Bowen WD. Sigma receptors: recent advances and new clinical potentials. Pharm Acta Helv 2000;7:211–8.

7. Maurice T, Urani A, Phan VL, Romieu P. The interaction between neuroactive steroids and the sigma₁ receptor function: behavioral consequences and therapeutic opportunities. Brain Res Rev 2001;37:116–32.

8. Hiramatsu M, Hoshino T, Kameyama T, Nabeshima T. Involvement of kappa-opioid and sigma receptors in short-term memory in mice. Eur J Pharmacol 2002;453:91–8.

9. Maurice T, Hiramatsu M, Kameyama T, Hasegawa T, Nabeshima T. Behavioral evidence for a modulating role of sigma ligands in memory processes. II. Reversion of carbon monoxide-induced amnesia. Brain Res 1994;647:57–64.

10. Senda T, Matsuno K, Okamoto K, Kobayashi T, Nakata K, Mita S. Ameliorating effect of SA4503, a novel sigma₁ receptor agonist, on memory impairments induced by cholinergic dysfunction in rats. Eur J Pharmacol 1996;315:1–10.

11. Matsuno K, Matsunaga K, Senda T, Mita S. Increase in extra-cellular acetylcholine level by sigma ligands in rat frontal cortex. J Pharmacol Exp Ther 1993;265:851–9.

12. Matsuno K, Senda T, Kobayashi T, Mita S. Involvement of sigma₁ receptor in (+)-N-allylnormetazocine-stimulated hippocampal cholinergic functions in rats. Brain Res 1995;690: 200–6.

13. Kobayashi T, Matsuno K, Nakata K, Mita S. Enhancement of acetylcholine release by SA4503, a novel sigma₁ receptor agonist, in the rat brain. J Pharmacol Exp Ther 1996;279: 106–13.

14. Ishiwata K, Kobayashi T, Kawamura K, Matsuno K. Age-related changes of the binding of [³H]SA4503 to sigma₁ receptors in the rat brain. Ann Nucl Med 2003;17:73–7.

15. Kawamura K, Kimura Y, Tsukada H, Kobayashi T, Nishiyama S, Kakiuchi T, et al. An increase of sigma receptors in the aged monkey brain. Neurobiol Aging 2003;24:745–52.

16. Weissman AD, Casanova MF, Kleinman JE, London ED, De Souza EB. Selective loss of cerebral cortical sigma, but not PCP binding sites in schizophrenia. Biol Psychiatry 1991;29: 41–54.

17. Matsuno K, Kobayashi T, Tanaka MK, Mita S. Sigma₁ receptor subtype is involved in the relief of behavioral despair in the mouse forced swimming test. Eur J Pharmacol 1996;312: 267–71.

18. Lobner D, Lipton P. Sigma-ligands and non-competitive NMDA antagonists inhibit glutamate release during cerebral ischemia. Neurosci Lett 1990;117:169–74.

19. Mishina M, Ishiwata K, Ishii K, Kitamura S, Kimura Y, Kawamura K, et al. Function of sigma receptors in Parkinson's disease. Acta Neurol Scand 2005;112:103–7.

20. Jansen KL, Faull RL, Storey P, Leslie RA. Loss of sigma binding sites in the CA1 area of the anterior hippocampus in Alzheimer's disease correlates with CA1 pyramidal cell loss. Brain Res 1993;623:299–302.

21. Maurice T. Improving Alzheimer's disease-related cognitive deficits with sigma₁ receptor agonists. Drug News Perspect 2002;15:617–25.

22. Ishiwata K, Tsukada H, Kawamura K, Kimura Y, Nishiyama S, Kobayashi T, et al. Mapping of CNS sigma₁ receptors in the conscious monkey: preliminary PET study with [¹¹C]SA4503. Synapse 2001;40:235–7.

23. Kawamura K, Ishiwata K, Tajima H, Ishii S, Matsuno K, Homma Y, et al. In vivo evaluation of [¹¹C]SA4503 as a PET ligand for mapping CNS sigma₁ receptors. Nucl Med Biol 2000;27:255–61.

24. Sakata M, Kimura Y, Naganawa M, Oda K, Ishii K, Chihara K, et al. Mapping of human cerebral sigma₁ receptors using positron emission tomography and [¹¹C]SA4503. Neuroimage 2007;35:1–8.

25. McKhann G, Drachman D, Folstein M, Katzman R, Price D, Stadlan EM. Clinical diagnosis of Alzheimer's disease: report of the NINCDS-ADRDA Work Group under the auspices of Department of Health and Human Services Task Force on Alzheimer's Disease. Neurology 1984;34:939–44.

26. Herholz K, Salmon E, Perani D, Baron JC, Holthoff V, Frolich L, et al. Discrimination between Alzheimer dementia and controls by automated analysis of multicenter FDG PET. Neuroimage 2002;17:302–16.

27. Minoshima S, Giordani B, Berent S, Frey KA, Foster NL, Kuhl DE. Metabolic reduction in the posterior cingulate cortex in very early Alzheimer's disease. Ann Neurol 1997;42: 85–94.

28. Reisberg B, Borenstein J, Salob SP, Ferris SH, Franssen E, Georgotas A. Behavioral symptoms in Alzheimer's disease: phenomenology and treatment. J Clin Psychiatry 1987;48 Suppl:9–15.

29. Folstein MF, Folstein SE, McHugh PR. "Mini-Mental State". A practical method for grading the cognitive state of patients for the clinician. J Psychiatr Res 1975;12:189–98.

30. Hughes CP, Berg L, Danziger WL, Coben LA, Martin RL. A new clinical scale for the staging of dementia. Br J Psychiatry 1982;140:566–72.

31. Fujiwara T, Watanuki S, Yamamoto S, Miyake M, Seo S, Itoh M, et al. Performance evaluation of a large axial field-of-view PET scanner: SET-2400 W. Ann Nucl Med 1997;11: 307–13.

32. Mishina M, Senda M, Kimura Y, Toyama H, Ishiwata K, Ohyama M, et al. Intrasubject correlation between static scan and distribution volume images for [¹¹C]flumazenil PET. Ann Nucl Med 2000;14:193–8.

33. Logan J. A review of graphical methods for tracer studies and strategies to reduce bias. Nucl Med Biol 2003;30:833–44.

34. Mielke R, Schroder R, Fink GR, Kessler J, Herholz K, Heiss WD. Regional cerebral glucose metabolism and postmortem pathology in Alzheimer's disease. Acta Neuropathol (Berl) 1996;91:174–9.

35. Ohyama M, Senda M, Ishiwata K, Kitamura S, Mishina M, Ishii K, et al. Preserved benzodiazepine receptors in Alzheimer's disease measured with C-11 flumazenil PET and I-123 iomazenil SPECT in comparison with CBF. Ann Nucl Med 1999;13:309–15.

36. Nordberg A. PET imaging of amyloid in Alzheimer's disease. Lancet Neurol 2004;3:519–27.

37. Braak H, Braak E, Bohl J, Lang W. Alzheimer's disease: amyloid plaques in the cerebellum. J Neurol sci 1989;93: 277–87.

38. Ishii K, Sasaki M, Kitagaki H, Yamaji S, Sakamoto S, Matsuda K, et al. Reduction of cerebellar glucose metabolism in advanced Alzheimer's disease. J Nucl Med 1997;38:925–8.

39. Larner AJ. The cerebellum in Alzheimer's disease. Dement Geriatr Cogn Disord 1997;8:203–9.

40. Wegiel J, Wisniewski HM, Dziewiatkowski J, Badmajew E, Tarnawski M, Reisberg B, et al. Cerebellar atrophy in Alzheimer's disease-clinicopathological correlations. Brain Res 1999;818:41–50.

41. Sjöbeck M, Englund E. Alzheimer's disease and the cerebellum: a morphologic study on neuronal and glial changes. Dement Geriatr Cogn Disord 2001;12:211–8.

42. Verdile G, Gnjec A, Miklossy J, Fonte J, Veurink G, Bates K, et al. Protein markers for Alzheimer disease in the frontal cortex and cerebellum. Neurology 2004;63:1385–92.

43. Sultana R, Boyd-Kimball D, Poon HF, Cai J, Pierce WM, Klein JB, et al. Redox proteomics identification of oxidized proteins in Alzheimer's disease hippocampus and cerebellum: an approach to understand pathological and biochemical alterations in AD. Neurobiol Aging 2006;27:1564–76.

44. Chaki S, Okuyama S, Ogawa S, Tomisawa K. Regulation of NMDA-induced [^{3}H]dopamine release from rat hippocampal slices through sigma-1 binding sites. Neurochem Int 1998;33: 29–34.

Robust estimation of the arterial input function for Logan plots using an intersectional searching algorithm and clustering in positron emission tomography for neuroreceptor imaging

Mika Naganawa,[a,b] Yuichi Kimura,[a,*] Junichi Yano,[c] Masahiro Mishina,[d] Masao Yanagisawa,[c] Kenji Ishii,[e] Keiichi Oda,[e] and Kiichi Ishiwata[e]

[a]Molecular Imaging Center, National Institute of Radiological Sciences, 4-9-1, Anagawa, Inage, Chiba-shi, Chiba, 263-8555, Japan
[b]Yale PET Center, School of Medicine, Yale University, New Haven, CT, USA
[c]Graduate School of Science and Engineering, Waseda University, Tokyo, Japan
[d]Neurological Institute, Nippon Medical School Chiba-Hokusoh Hospital, Chiba, Japan
[e]Positron Medical Center, Tokyo Metropolitan Institute of Gerontology, Tokyo, Japan

The Logan plot is a powerful algorithm used to generate binding-potential images from dynamic positron emission tomography (PET) images in neuroreceptor studies. However, it requires arterial blood sampling and metabolite correction to provide an input function, and clinically it is preferable that this need for arterial blood sampling be obviated. Estimation of the input function with metabolite correction using an intersectional searching algorithm (ISA) has been proposed. The ISA seeks the input function from the intersection between the planes spanned by measured radioactivity curves in tissue and their cumulative integrals in data space. However, the ISA is sensitive to noise included in measured curves, and it often fails to estimate the input function. In this paper, we propose a robust estimation of the cumulative integral of the plasma time–activity curve (pTAC) using ISA (robust EPISA) to overcome noise issues. The EPISA reduces noise in the measured PET data using averaging and clustering that gathers radioactivity curves with similar kinetic parameters. We confirmed that a little noise made the estimation of the input function extremely difficult in the simulation. The robust EPISA was validated by application to eight real dynamic [^{11}C]TMSX PET data sets used to visualize adenosine A_{2A} receptors and four real dynamic [^{11}C]PIB PET data sets used to visualize amyloid-beta plaque. Peripherally, the latter showed faster metabolism than the former. The clustering operation improved the signal-to-noise ratio for the PET data sufficiently to estimate the input function, and the calculated neuroreceptor images had a quality equivalent to that using measured pTACs after metabolite correction. Our proposed method noninvasively yields an alternative input function for Logan plots, allowing the Logan plot to be more useful in neuroreceptor studies.
© 2007 Elsevier Inc. All rights reserved.

Keywords: Positron emission tomography; Clustering; Intersectional searching algorithm; Arterial blood sampling; Logan plot

Introduction

The Logan plot (Logan et al., 1990) is a graphical approach that estimates volume of distribution (V_T) from the slope of a plot. V_T refers to the sum of the volume of distributions in the free, nonspecific binding, and specific binding compartments (Koeppe et al., 1991; Innis et al., 2007). Because this algorithm achieves more robust and faster estimation compared with nonlinear least squares methods (Carson, 2002), it is widely used for generating parametric images of V_T in neuroreceptor mapping. The Logan plot requires two measurable data sets: one is obtained by dynamic PET scanning, and the other is obtained by serial arterial blood sampling. If the serial arterial blood sampling can be omitted, the Logan plot becomes a more useful and easy-to-use approach. There are several approaches to avoiding invasive arterial blood sampling. Reference-region-based Logan plot (Logan et al., 1996) cancels out the term of the integral of the plasma time–activity curve (pTAC) using a tissue time–activity curve (tTAC) in reference regions where the target receptor is negligible. Although the term relating to the pTAC is expelled, the estimation equation still includes an efflux parameter, k_2 [1/min]. It is sometimes difficult to know the value of k_2 about reference regions in advance. If an equilibrium state is achieved between tTAC and pTAC, a priori knowledge of k_2 is not necessary, but such a

* Corresponding author.
E-mail address: ukimura@ieee.org (Y. Kimura).
Available online on ScienceDirect (www.sciencedirect.com).

situation is not always realized. Another approach, which we have previously proposed, is based on a statistical model: independent component analysis (Naganawa et al., 2005a,b) and variational Bayes (Naganawa et al., 2007a). These methods assume a factor analysis model in which each voxel includes the radioactivities from tissue and blood, and estimates the time–activity curve (TAC) of whole blood radioactivity. The estimated blood curve was successfully used in Logan plots as an alternative to the measured pTAC. Note that the plasma-to-whole blood ratio should be constant in the time for which the Logan plot was applied (Naganawa et al., 2005b), and the estimated blood curve includes the radioactivity in metabolites.

In applying the Logan plot, an input blood function appears in a form of the cumulative integral of the pTAC (intpTAC). It is desirable for the intpTAC to be corrected metabolically. Wang et al. proposed an intersectional searching algorithm (ISA) to estimate the intpTAC directly (Wang et al., 2005). The metabolite-corrected intpTAC will be theoretically obtained using their algorithm. However, one aspect to be considered is noise in the measured tTACs. Because of its mathematical nature, the ISA is very sensitive to noise, and it is thus important to reduce the noise effectively in estimating intpTAC. We have developed methods to reduce the measurement noise using clustering based on each TAC's kinetics (Kimura et al., 1999, 2005a,b). It is expected that our clustering method will improve estimation using ISA. In this paper, we propose a method for robust extraction of the intpTAC using ISA and clustering (robust EPISA). We clarify the sensitivity of the ISA to the measurement noise using simulations, and we investigate the applicability of the robust EPISA by applying it to dynamic PET data using [7-methyl-^{11}C]-(E)-8-(3,4,5-trimethoxystyryl)-1,3,7-trimethylxanthine ([^{11}C]TMSX), which visualizes adenosine A_{2A} receptors (Ishiwata et al., 2000, 2005; Mishina et al., 2007), and [N-methyl-^{11}C]2-(4'-methylaminophenyl)-6-hydroxy-benzothiazole] ([^{11}C]PIB), which visualizes amyloid-beta plaque (Mathis et al., 2003; Klunk et al., 2004).

Theory

ISA

ISA (Wang et al., 2005) estimates the intpTAC using at least two tTACs with mutually different shapes and the corresponding cumulative integral of the tTACs (inttTAC) based on the equations for the Logan plot. This section provides an overview of the ISA and discusses its drawbacks. The equation for the Logan plot is described as

$$
\frac{\int_0^T c^{(i)}(t)dt}{c^{(i)}(T)} = d^{(i)} \frac{\int_0^T c_p(t)dt}{c^{(i)}(T)} + b^{(i)}.
\tag{1}
$$

where $c^{(i)}(t)$ is a tTAC at the ith voxel or region and $c_p(t)$ is a pTAC. $\int_0^T c^{(i)}(t)dt$ and $\int_0^T c_p(t)dt$ are inttTAC at the ith voxel and intpTAC, respectively. For time $T \geq t^*$, the second term $b^{(i)}$ (<0) is a constant, and $d^{(i)}$ corresponds to a V_T. Eq. (1) is arranged for $\int_0^T c_p(t)dt$ as

$$
\int_0^T c_p(t)dt = \frac{-b^{(i)}}{d^{(i)}} c^{(i)}(T) - \frac{1}{d^{(i)}} \int_0^T c^{(i)}(t)dt
$$
$$
= a_1^{(i)} c^{(i)}(T) + a_2^{(i)} \int_0^T c^{(i)}(t)dt.
\tag{2}
$$

Because the values of $d^{(i)}$ and $b^{(i)}$ are constant, constant coefficients $b^{(i)}/d^{(i)}$ and $1/d^{(i)}$ are denoted as $a_1^{(i)}$ and $a_2^{(i)}$, respectively. Assuming that a tTAC is measured at times $T = t_1, t_2, \ldots, t_m$, Eq. (2) can be written in terms of vectors as

$$
c_{pint} = a_1^{(i)} c^{(i)} + a_2^{(i)} c_{int}^{(i)}
\tag{3}
$$

where c_{pint}, $c^{(i)}$, and $c_{int}^{(i)}$ are column vectors of m elements corresponding to $\int_0^T c_p(t)dt$, $c^{(i)}(T)$, and $\int_0^T c^{(i)}(t)dt$, respectively. Because c_{pint} is a common vector between the ith and jth voxels or regions $(i \neq j)$, the following equation is obtained.

$$
a_1^{(i)} c^{(i)} + a_2^{(i)} c_{int}^{(i)} = a_1^{(j)} c^{(j)} + a_2^{(j)} c_{int}^{(j)}
\tag{4}
$$

Eq. (4) can be rewritten as

$$
(c^{(i)} c_{int}^{(i)} c^{(j)} c_{int}^{(j)}) \begin{pmatrix} a_1^{(i)} \\ a_2^{(i)} \\ -a_1^{(j)} \\ -a_2^{(j)} \end{pmatrix} = Ca = 0.
\tag{5}
$$

where $C \in \mathcal{R}^{m \times 4}$ is a matrix $(m > 4)$ and $a \in \mathcal{R}^{4 \times 1}$ is a column vector. Because the rank of the matrix C is at most three, the vector a can be estimated as a right singular vector corresponding to the smallest right singular value of C. Because any vector whose direction is equal to the right singular vector a satisfies Eq. (5), the length of a cannot be determined. Accordingly, the absolute value of the intpTAC cannot be determined. ISA infers only the shape of the intpTAC during the period in which the Logan plot can be applied. Although the absolute value of the V_T at each voxel cannot be determined using the Logan plot with ISA-estimated intpTAC, the ratio between them can be estimated. Note that the estimation of the intpTAC is limited to the range of time used for the Logan plot, because ISA is defined only on the frames where the Logan plot is applicable. Thus, ISA is useless in estimating the intpTAC at early times, and the estimated intpTAC cannot be used as an input function for the nonlinear least squares method.

Let us give a geometrical interpretation of ISA algorithm to allow intuitive understanding of the effect of noise. Eq. (3) means that the intpTAC vector c_{pint} is on the plane that is spanned by the tTAC vector $c^{(i)}$ and the inttTAC vector $c^{(i)}$. Eq. (4) shows that c_{pint} is an intersectional vector of two planes by the i and jth voxel. Fig. 1 shows the geometric relationship between intpTAC, the tTACs and the inttTACs. In reality, there is a large amount of noise in the measured PET data. Therefore, the plane spanned by the tTAC vector and the inttTAC vector is deviated from the true plane. Accordingly, the measurement noise produces estimation error in the direction of the intersectional vector c_{pint}.

Robust EPISA

The proposed method, robust EPISA, improves the signal-to-noise ratio of the measured PET data using averaging and clustering. The voxels that locate close to each other tend to have similar kinetics. In addition, there exist tTACs that have similar kinetics but locate at separate positions. In robust EPISA, first, a spatial averaging filter is applied. Clustering is subsequently performed to gather tTACs based on their kinetics, and tTACs classified into the same cluster are averaged. Finally,
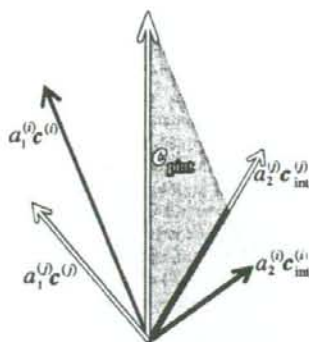
Fig. 1. Schematic illustration of a relationship between intpTAC, the tTACs, and the inttTACs. The intpTAC is estimated as an intersection vector of two planes.

the intersection-searching algorithm is applied to noise-reduced data.

To reduce noise, clustering was performed using a quantity proposed in (Kimura et al., 1999, 2002). The quantity, R, is defined as

$$R = \frac{\int_0^T c^{(i)}(t)\,dt}{\int_0^T t c^{(i)}(t)\,dt} \tag{6}$$

where T is the time of the final frame. The amplitude of R is determined by only the shape of the tTAC emphasized by t. The quantity R is invariant when the tTAC becomes the product of a constant α times the tTAC $c^{(i)}(t)$, because α is canceled out between the numerator and the denominator in Eq. (6). Therefore, the quantity R evaluates the tTAC's shape. For example, the quantity R becomes a function of a kinetic efflux parameter k_2 when a kinetic of the administered radioligand is described by a one-tissue two-compartment model (Kimura et al., 1999).

The actual procedures in robust EPISA are shown below.

1. The region outside the brain was excluded and voxel-based PET data were spatially averaged.
2. The quantity, R, was calculated about each voxel, and voxels with similar R were categorized into one cluster. The same number of voxels were assigned to each cluster.
3. The tTACs categorized into the same cluster were averaged. Note that each tTAC was normalized by each time integral.
4. The intpTACs were estimated from all possible pairs of the averaged tTACs.
5. The candidate intpTACs were obtained from all estimated intpTACs by excluding failed curves, and the final result was the averaged candidate intpTACs.

A suitable size of clusters for Step 2 was investigated. An intpTAC should be a monotonically increasing function with positive values. The failed curves in Step 5 mean the intpTACs with negative values or the intpTACs that do not monotonically increase. In Step 5, a scale of the intpTAC should be normalized before averaging because it cannot be determined using ISA.

Materials and methods

Simulations

Simulations were carried out to investigate the behavior of the ISA in the presence of noise to make sure of the necessity of noise reduction in applying ISA. Perfect tTACs were generated using a metabolite-corrected pTAC obtained from a human [¹¹C]TMSX study with serial arterial blood sampling. Kinetic parameter values of [¹¹C]TMSX in the putamen and the frontal lobe (Naganawa et al., 2007b) were chosen for the generation of noise-free tTACs ($K_1 = 0.32$ (mL plasma)·min⁻¹ (mL tissue)⁻¹, $k_2 = 0.43$ min⁻¹, $k_3 = 0.44$ min⁻¹, $k_4 = 0.36$ min⁻¹ and $K_1 = 0.29$ (mL plasma)·min⁻¹ (mL tissue)⁻¹, $k_2 = 0.39$ min⁻¹, $k_3 = 0.13$ min⁻¹, $k_4 = 0.29$ min⁻¹, respectively). Noisy tTACs were subsequently obtained by adding Gaussian noise to the noise-free data. Added noise was expressed as $\mathcal{N}\left(0, \beta \frac{c(t)}{\Delta t}\right)$, where Δt is the frame width and β is a proportional constant that represents the noise level. The simulations were conducted for a protocol of 27 frames over a period of 1 h ($10\,s \times 6$, $30\,s \times 3$, $60\,s \times 5$, $150\,s \times 5$, and 5 min×8). The noise level β was set to be 0 and 16. The noise level was scaled so that the value of 16 corresponded to the averaged tTAC over 100 voxels. In the simulation, 20 realizations of noisy tTACs were generated, and 10 pairs of tTACs were randomly selected from the tTACs, and ISA was applied to them because an intpTAC is estimated using two tTACs in EPISA. ISA was also applied to noise-free tTACs. Because it is possible to apply Logan plots to [¹¹C]TMSX 10 min after administration (Naganawa et al., 2007b), ISA was performed using the simulated data between 27.5 and 57.5 min after administration. The estimated intpTACs were compared with the true intpTAC.

[¹¹C]TMSX PET studies

The presented method (robust EPISA) was applied to eight human [¹¹C]TMSX PET data sets in order to investigate the effects of averaging and clustering. The Ethics Committee of Tokyo Metropolitan Institute of Gerontology approved the study protocol. [¹¹C]TMSX PET data were acquired from seven healthy volunteers and one patient with Parkinson's disease. Written informed consent was obtained from all subjects before the study. After a transmission scan, 590–103 MBq of [¹¹C]TMSX with a specific activity of 40 ± 21 GBq/μmol was administered intravenously, and a 1 h dynamic PET scan was performed in two-dimensional mode using a SET-2400W (Shimadzu Co., Kyoto, Japan). The acquisition consisted of 27 frames of data (10 s × 6, 30 s × 3, 60 s × 5, 150 s × 5, and 5 min × 8). The dynamic PET data were reconstructed using a filtered back-projection algorithm with a second-order low-pass filter with a cutoff frequency of 1.25 cycles/cm. Twenty-five slices were scanned—each slice with 96 × 96 voxels—and the resulting voxel size was $2 \times 2 \times 6.25$ mm. Serial arterial blood sampling and metabolite analysis were performed during the scan. Arterial blood samples were taken from the brachial artery at 10, 20, 30, 40, 50, 60, 70, 80, 90, 100, 110, 120, 135 and 150 s and 3, 5, 7, 10, 15, 20, 30, 40, 50 and 60 min. The radioactivity in the plasma was measured using a well-type gamma counter (BSS-1, Shimadzu Co., Kyoto, Japan) against which the PET camera was cross-calibrated. The unmetabolized fraction was measured by high-performance liquid chromatography (Ishiwata et al., 2003). The unmetabolized fraction in the plasma samples was fitted to the function proposed in Watabe et al. (2000).

Fifteen slices that cover the whole brain were used for estimation by robust EPISA. The regions outside the brain were specified as the voxels below the 70th percentile of the summed PET images and were excluded from the target of the robust EPISA. Approximately 63,000 voxels were used for the estimation. The 5-by-5 average filter was applied to the measured PET images to improve the signal-to-noise ratio by spatial averaging. The number of clusters was set to 50, and approximately 1250 voxels were included in one cluster. Thus, sufficiently noise-reduced tTACs were obtained. PET images taken between 27.5 and 57.5 min after administration were used in the ISA. The estimated intpTAC was divided by its value at the last frame for normalization. Logan plot was applied to obtain the V_T image using the metabolite-corrected intpTAC and the estimated intpTAC. The centrum semiovale was manually defined as a reference region, and the binding potential, BP_{ND}, image was given by $\frac{V_T}{V_{ND}} - 1$ where V_{ND} is the averaged V_T over the centrum semiovale.

[^{11}C]PIB PET studies

The peripheral metabolism of [^{11}C]TMSX is slow; more than 95% of administered [^{11}C]TMSX remains as the intact form at 60 min post injection (Naganawa et al., 2007b). Therefore, the measured pTACs with and without metabolite correction have similar shape in [^{11}C]TMSX data. In order to investigate the influence of metabolites included in plasma and the number of clusters, the robust EPISA was also applied to four human [^{11}C] PIB PET data sets with faster metabolism. Parent fraction of [^{11}C] PIB was $48 \pm 13\%$ at 20 min and $30 \pm 8\%$ at 60 min post injection. The Ethics Committee of Tokyo Metropolitan Institute of Gerontology approved the study protocol. [^{11}C]PIB PET data were acquired from two healthy volunteers and two patients with Alzheimer disease who met the criteria of probable AD by NINDS-ADRDA and Dementia of Alzheimer's Type with DSM-IV. Written informed consent was obtained from all subjects before the study. After a transmission scan, 455 ± 55 MBq of [^{11}C]PIB with a specific activity of 88 ± 32 GBq/μmol was administered intravenously, and a 1 h dynamic PET scan was performed in three-dimensional mode using the same scanner as [^{11}C]TMSX scan. The acquisition consisted of 23 frames of data (10 s×6, 20 s×3, 60 s×2, 2 min×1, 4 min×1, and 5 min×10). Image reconstruction, serial arterial blood sampling and metabolite analysis were conducted in the same way as [^{11}C]TMSX scan, and 50 slices were scanned.

Slices that cover the whole brain were used for estimation by robust EPISA. The regions outside the brain were specified as the voxels below the 80th percentile of the summed PET images and were excluded from the target of the robust EPISA. Approximately 126,000 voxels were used for the estimation. The 9-by-9 average filter was applied to the measured PET images. The number of clusters was set to 10 (12,600 voxels/cluster), 20 (6300 voxels/ cluster), 40 (3150 voxels/cluster) and 80 (1575 voxels/cluster). ISA was applied to PET images taken between 37.5 and 57.5 min after administration (Price et al., 2005; Lopresti et al., 2005). The estimated intpTAC was divided by its value at the last frame for normalization. Logan plot was applied to obtain the V_T image using the metabolite-corrected intpTAC and the estimated intpTAC. The cerebellum was manually defined as a reference region (Price et al., 2005), and the distribution volume ratio (DVR) image was calculated.

Results

Simulation

The noise sensitivity of the ISA was confirmed using the simulated [^{11}C]TMSX data. The noise-free tTACs and examples of noise-added tTACs used for the simulation are presented in Fig. 2. Fig. 3 shows the estimated intpTACs and the true intpTAC. The scale was adjusted so that the value at the last frame corresponds to that of the true intpTAC. There was no difference between the ISA-estimated intpTAC and the true intpTAC with noise-free data. However, the estimated intpTACs were apparently deviated from the true intpTAC with a noise level of 16.

[^{11}C]TMSX PET studies

Clustering results are shown in Figs. 4 and 5. In Fig. 5, the voxels that have larger clustering criterion R are represented in a brighter color. While the neighboring voxels tend to belong to the same cluster and brain structure can be observed in Fig. 5, some remote voxels were also categorized into the same cluster. The intpTAC was estimated from the clustered and averaged tTACs as shown in Fig. 4. The noise level in the cluster-averaged tTACs was well suppressed. The estimated intpTACs using the proposed robust EPISA is demonstrated with standard deviation in Fig. 6(A). Note that standard deviation was not calculated from all estimated intpTACs but the candidate intpTACs as described in Step 5 in the Robust EPISA section. The estimated intpTACs were similar to the measured intpTACs with metabolite correction. The scale of the robust EPISA estimated intpTAC cannot be determined. In order to compare the estimated intpTACs with the measured intpTACs, the estimated intpTACs were scaled using the value at the last frame. The measured intpTACs without metabolite correction were also scaled using the value at the last frame. It took 5 to 7 s to estimate the intpTAC from one subject's data. The Logan plot was applied to the measured PET data to generate the V_T parametric images, and Fig. 7 shows BP_{ND} images calculated using the estimated V_T
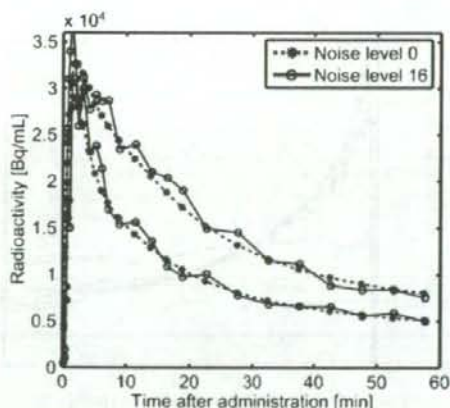

Fig. 2. Example of noise-free tTACs (dashed lines) and noisy tTACs (solid lines) for the simulation investigating the influence of noise in tTACs. The noise level of the noisy tTACs was set to 16. Two kinds of tTACs were used for estimation using ISA.
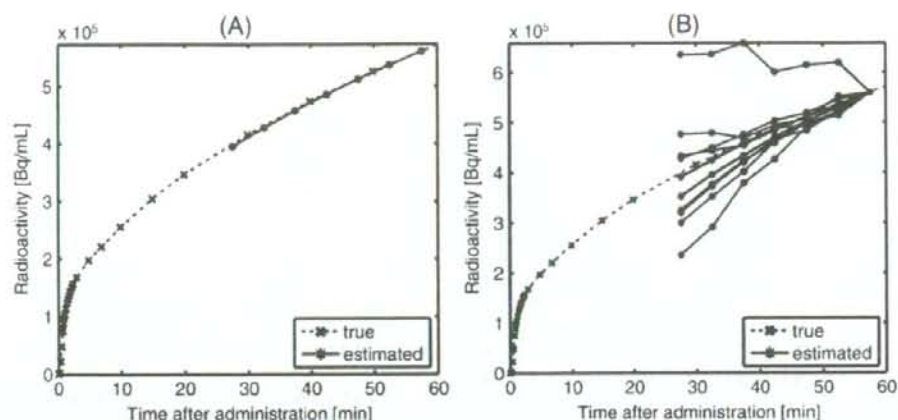
Fig. 3. Estimated intpTACs from the noise-free data (A) and the noisy data (B). The period used for the ISA was 27.5 min to 57.5 min after administration. The true intpTAC was obtained by cumulatively integrating the true pTAC. The estimated intpTACs are shown as solid lines, and the true intpTACs are shown as dashed lines. The scale of the estimated intpTAC was adjusted using the value at the last frame.

parametric images and the specified reference region. The BP_{ND} images with the estimated and measured intpTACs matched well in all eight subjects. In the linear regression between the measured and estimated BP_{ND} images, the slopes and y-intercepts were 1.00 ± 0.011 and 0.035 ± 0.016, respectively. The coefficient of determination (r^2) was 1.00 ± 0.0016.

[^{11}C]PIB PET studies

Fig. 6(B) shows the estimated intpTAC and the standard deviation calculated from candidate intpTACs. The estimated intpTACs were similar to the measured intpTACs with metabolite correction. For comparison, the scale of the estimated intpTACs and the measured intpTACs without metabolite correction was adjusted using the value at the last frame of the measured intpTACs

with metabolite correction. The calculation time was comparable to [^{11}C]TMSX study. The relationship between the number of clusters and estimation results were demonstrated in Fig. 8. Standard deviation increased as the size of the clusters became smaller. However, the final estimated intpTAC was little influenced by the choice of the number of clusters. In each case with different number of clusters, the candidate intpTACs from which the final result was obtained were approximately 22% curves out of all estimated intpTACs. When the number of the clusters set to be less than 5, the proposed method did not work. The Logan plot was applied to the measured PET data to generate the V_T parametric images, and Fig. 9 shows the DVR images of Alzheimer disease patient that were calculated using the estimated V_T parametric images in case of 20 clusters. The DVR images with the estimated and measured intpTACs matched well in all four subjects. In the linear regression between the measured and estimated DVR images, the slopes and y-intercepts were 0.97 ± 0.038 and 0.060 ± 0.057, respectively. The coefficient of determination (r^2) was 0.97 ± 0.026.

Discussion

The proposed method, robust EPISA, settles the mathematical drawback in ISA, in that performance is influenced by the noise in the measured tTACs. The measurement noise included in PET data was reduced by clustering based on tTAC's kinetics, and an input function for Logan plots was estimated robustly based on ISA (Wang et al., 2005). Robust EPISA estimates a shape of a cumulative integral curve of pTAC appearing in the operational equation of the Logan plot, and enables binding-potential imaging to be generated with no arterial blood sampling or metabolite correction. Omission of arterial blood sampling reduces the invasiveness of PET measurement and contributes to the shortened total time needed for preparation of serial arterial blood sampling. Before discussing the robustness of the proposed method, we should consider the advantages and disadvantages of ISA.

ISA has two advantages: no requirement for metabolite correction of pTAC and wide applicability to PET data with various radioligands, because of the broad application of the Logan
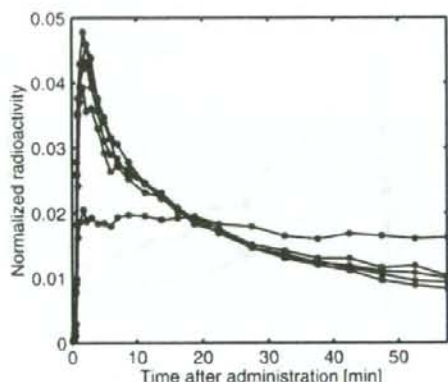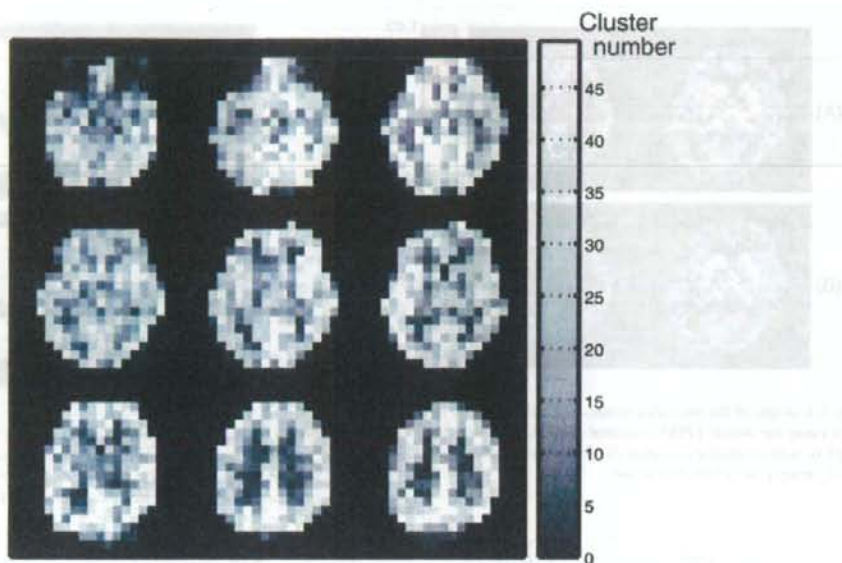

Fig. 4. Representative tTACs after clustering in [^{11}C]TMSX data. The tTACs of the measured PET data were categorized into 50 clusters and subsequently averaged in each cluster. Each tTAC was normalized by dividing by its integral.

Fig. 5. Example of a clustered image in [¹¹C]TMSX data. The voxel value corresponds to the cluster number. As the cluster number becomes larger, the corresponding criterion R also becomes larger.

plot. Many methods have been proposed to preclude arterial blood sampling. One of these methods is based on a factor model to estimate the shape of a whole blood curve (Barber, 1980; Paola et al., 1982; Wu et al., 1995; Lee et al., 2001; Naganawa et al., 2005a,b), where the radioactivity in the measured PET data is assumed to be the sum of the radioactivities in the blood and tissue. In this method, metabolite correction is unattainable. On the other hand, ISA can theoretically give a metabolite-corrected pTAC. ISA is derived from the operational equation for the Logan plot, and the

equations of the Logan plot are based on a compartment model. Thus, the estimated intpTAC does not include the radioactivity in metabolites. There is a great difference between the measured intpTAC with and without metabolite correction in [¹¹C]PIB data. The estimated intpTAC matched well with the measured intpTAC with metabolite correction as shown in Fig. 6. From our results, the estimated BP_{ND} of [¹¹C]TMSX (Fig. 7) or DVR of [¹¹C]PIB (Fig. 9) using the proposed method coincide well with those using a measured pTAC with metabolite correction. It is expected that ISA
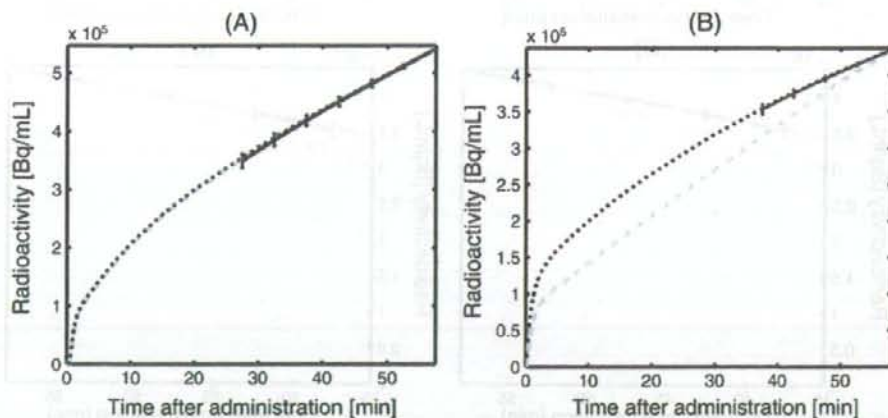

Fig. 6. Example of a robust EPISA-estimated intpTAC (black solid line) in (A) [¹¹C]TMSX and (B) [¹¹C]PIB. In [¹¹C] PIB, 40 clusters were used for clustering. Measured intpTACs with and without metabolite correction were plotted in black dotted line and gray break line, respectively. Standard deviation was calculated from the candidate intpTACs.
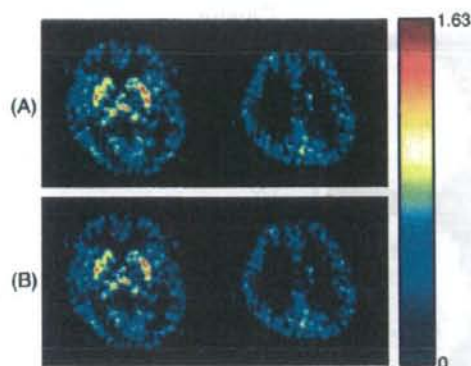
Fig. 7. Example of the parametric images of the BP_{ND} in [^{11}C]TMSX PET data using the robust EPISA-estimated intpTAC (A) and the measured intpTAC with metabolite correction (B). These images were calculated from the V_1 images and a reference region.
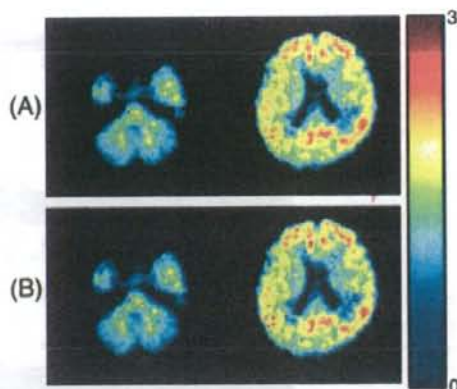

Fig. 9. Example of the parametric images of [^{11}C]PIB DVR in brain with Alzheimer disease. These images were calculated from the V_1 images and a reference region using the robust EPISA-estimated intpTAC (A) and the measured intpTAC with metabolite correction (B).
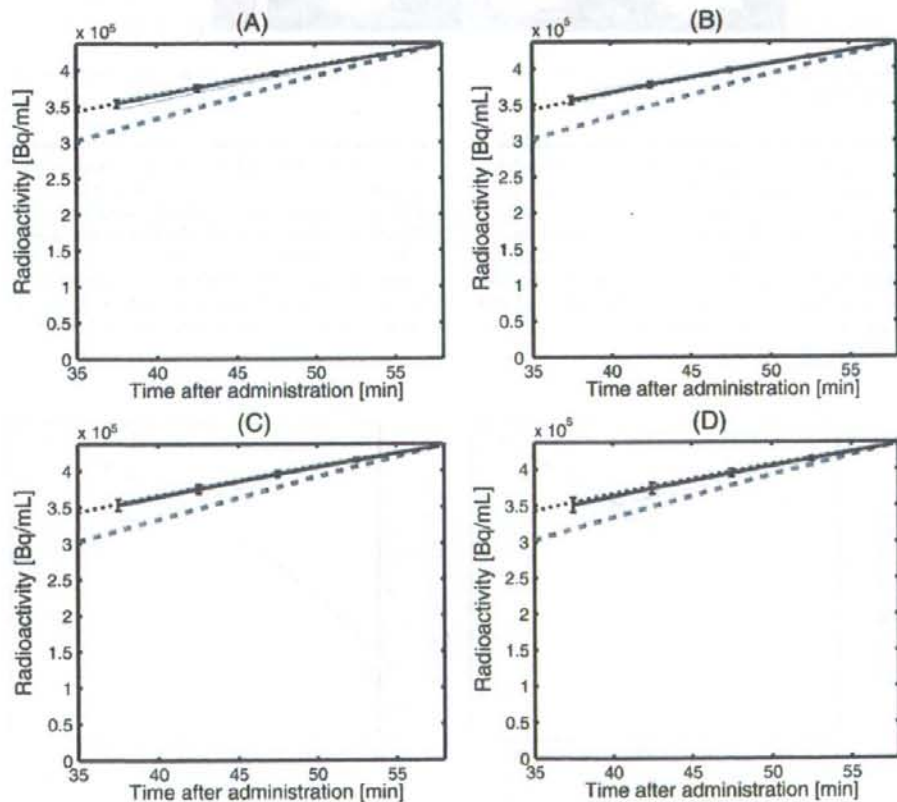

Fig. 8. Typical example of robust EPISA-estimated intpTACs (black solid line) in [^{11}C]PIB. The number of clusters was set to (A) 10, (B) 20, (C) 40, and (D) 80. Measured intpTACs with and without metabolite correction were plotted in black dotted line and gray break line. Standard deviation was calculated from the candidate intpTACs that were shown in gray solid lines.

will be applicable to radiopharmaceuticals whose metabolites cannot be ignored, or PET data with metabolism varied because of disease, dose, or other pathophysiological situations.

The next issue is the wide applicability of ISA. Using ISA, parametric images of BP_{ND} can be calculated using the estimated intpTAC and the specified reference region. When arterial blood sampling is not available, the basis function method (Gunn et al., 1997) is commonly used. While the basis function method is appropriate only when the PET data is described by a simplified reference tissue model (Lammertsma and Hume, 1996), ISA can be applied to any PET data with reversibly binding tracers. In this paper, to assure the wide applicability, EPISA was applied to two radioligands: [¹¹C]TMSX with slow peripheral metabolism and [¹¹C]PIB with fast one.

ISA has a disadvantage in practical application because of its high sensitivity to measurement noise. ISA is an algorithm to estimate the intersection between the planes spanned by tTAC and inttTAC. As shown in Fig. 3, ISA failed in estimating the intpTAC, even with low-noise. The reason for this is considered here. The ISA algorithm leads to the singular value decomposition problem. Generally, the singular vector with the smallest singular value is inaccurately estimated in the presence of noise. Therefore, it is important to reduce noise from the measured PET data before applying ISA.

In addition, the absolute value of the intpTAC cannot be estimated using ISA, as with other mathematical algorithms for the pTAC estimation (Barber, 1980; Paola et al., 1982; Wu et al., 1995; Lee et al., 2001; Naganawa et al., 2005a,b), because only the direction of a singular vector is presumable. Therefore, the relative V_T is obtained using Logan plot with the estimated pTAC or intpTAC. At least one-point arterial blood sampling is required to scale the estimated pTAC or intpTAC and calculate the absolute V_T. However, BP_{ND} can be calculated from the ratio of V_T values between target voxels and the reference region, and this calculation does not require the absolute value of the intpTAC. ISA can form the parametric image of BP_{ND} by specifying reference region.

In this study, a kinetic model-based clustering scheme was applied for noise reduction. It has been successfully applied in the rapid and robust parametric imaging of regional cerebral blood flow (Kimura et al., 1999) and [¹⁸F]FDG studies (Kimura et al., 2002). In this paper, we proposed averaging and clustering as a way to successful ISA. The measured tTACs were clustered based on their kinetic shape. In the [¹¹C]TMSX studies, approximately 1250 voxels were assigned to a single cluster. Although the size of the cluster is too large as an anatomical ROI, such a large ROI is appropriate for EPISA because reducing noise is more important than increasing heterogeneity in the clusters. The estimated result was not influenced too much by the choice of the number of the clusters as shown in Fig. 8. IntpTACs were estimated from all possible pairs of the noise-reduced tTACs. In some pairs, estimated intpTACs were not monotonically increasing. The derivative of the intpTAC equals the pTAC. Therefore, the pTAC includes negative values when the intpTAC was not monotonically increasing.

The reference-region-based Logan plot also successfully estimates DVR or BP_{ND} without arterial blood sampling. Comparing EPISA with the reference-region-based Logan plot, robust EPISA does not need any kinetic parameters, while the reference-region-based Logan plot requires the population value of k_2 in the reference region in advance. We think that it is an advantage over the noninvasive Logan analysis. Note that noninvasive Logan analysis

and our method will provide comparable results when the values of k_2 in a reference region are sufficiently similar in all subjects.

Exact values should be specified for the set of parameters used in the robust EPISA: the size of the averaging filter and the number of clusters. When the PET data have a low signal-to-noise ratio, a larger averaging filter and fewer clusters are preferable. We conclude that the ISA is a practical algorithm for the obviation of arterial blood sampling using noise reduction with clustering.

Acknowledgments

References

Barber, D.C., 1980. The use of principal components in the quantitative analysis of gamma camera dynamic studies. Phys. Med. Biol. 25 (2), 283–292.

Carson, R.E., 2002. Positron Emission Tomography Basic Science and Clinical Practice. Springer, Ch. 6, pp. 147–179.

Gunn, R.N., Lammertsma, A.A., Hume, S.P., Cunningham, V.J., 1997. Parametric imaging of ligand–receptor in PET using a simplified reference region model. NeuroImage 6 (4), 279–287.

Innis, R.B., Cunningham, V.J., Delforge, J., Fujita, M., Gjedde, A., Gunn, R.N., Holden, J., Houle, S., Huang, S.-C., Ichise, M., Iida, H., Ito, H., Kimura, Y., Koeppe, R.A., Knudsen, G.M., Knuuti, J., Lammertsma, A.A., Laruelle, M., Logan, J., Maguire, R.P., Mintun, M.A., Morris, E.D., Parsey, R., Price, J.C., Slifstein, M., Sossi, V., Suhara, T., Votaw, J.R., Wong, D.F., Carson, R.E., 2007. Consensus nomenclature for in vivo imaging of reversibly binding radioligands. J. Cereb. Blood Flow Metab. 27 (9), 1533–1539.

Ishiwata, K., Ogi, N., Shimada, J., Nonaka, H., Tanaka, A., Suzuki, F., Senda, M., 2000. Further characterization of a CNS adenosine A₂ₐ receptor ligand [¹¹C]KF18446 with in vitro autoradiography and in vivo tissue uptake. Ann. Nucl. Med. 14 (2), 81–89.

Ishiwata, K., Wang, W.-F., Kimura, Y., Kawamura, K., Ishii, K., 2003. Preclinical studies on [¹¹C]TMSX for mapping adenosine A₂ₐ receptors by positron emission tomography. Ann. Nucl. Med. 17 (3), 205–211.

Ishiwata, K., Mishina, M., Kimura, Y., Oda, K., Sasaki, T., Ishii, K., 2005. First visualization of adenosine A₂ₐ receptors in the human brain by positron emission tomography with [¹¹C]TMSX. Synapse 55 (2), 133–136.

Kimura, Y., Hsu, H., Toyama, H., Senda, M., Alpert, N.M., 1999. Improved signal-to-noise ratio in parametric images by cluster analysis. NeuroImage 9 (5), 554–561.

Kimura, Y., Senda, M., Alpert, N.M., 2002. Fast formation of statistically reliable FDG parametric images based on clustering and principal components. Phys. Med. Biol. 47 (3), 455–468.

Kimura, Y., Naganawa, M., Yano, J., 2005a. Multidimensional clustering for molecular imaging using positron emission tomography and Logan plot to improve noise reduction capability. Proceedings of the International Federation for Medical and Biological Engineering, vol. 12, p. 2A2-01. Singapore.

Kimura, Y., Yano, J., Tsukahara, M., Naganawa, M., Ishii, K., Ishiwata, K., 2005b. Clustering approach for voxel-based Logan plot to improve noise reduction capability. VIIth International Conference on Quantification of Brain Function with PET. Amsterdam, Netherlands, p. S632.

Klunk, W.E., Engler, H., Nordberg, A., Wang, Y., Blomqvist, G., Holt, D.P., Bergström, M., Savitcheva, I., Huang, G.-F., Estrada, S., Ausén, B., Debnath, M.L., Barletta, J., Price, J.C., Sandell, J., Lopresti, B.J., Wall, A., Koivisto, P., Antoni, G., Mathis, C.A., Långström, B., 2004. Imaging brain amyloid in Alzheimer's disease with Pittsburgh Compound-B. Ann. Neurol. 55 (3), 306–319.

Koeppe, R.A., Holthoff, V.A., Frey, K.A., Kilbourn, M.R., Kuhl, D.E., 1991.

Compartmental analysis of [^{11}C]flumazenil kinetics for the estimation of ligand transport rate and receptor distribution using positron emission tomography. J. Cereb. Blood Flow Metab. 11 (5), 735 744.

Lammertsma, A.A., Hume, S.P., 1996. Simplified reference tissue model for PET receptor studies. NeuroImage 4, 153 158.

Lee, J.S., Lee, D.S., Ahn, J.Y., Cheon, G.J., Kim, S.K., Yeo, J.S., Seo, K., Park, K.S., Chung, J.K., Lee, M.C., 2001. Blind separation of cardiac components and extraction of input function from H$_2$^{15}O dynamic myocardial PET using independent component analysis. J. Nucl. Med. 42 (6), 938 943.

Logan, J., Fowler, J.S., Volkow, N.D., Wolf, A.P., Dewey, A.L., Schlyer, D.J., MacGregor, R.R., Hitzeman, R., Bendriem, B., Gatley, S.J., Christman, D.R., 1990. Graphical analysis of reversible radioligand binding from time activity measurements applied to [n-^{11}C-methyl]-(-)-cocaine PET studies in human subjects. J. Cereb. Blood Flow Metab. 10 (5), 740 747.

Logan, J., Fowler, J.S., Volkow, N.D., Wang, G.-J., Ding, Y.-S., Alexoff, D.L., 1996. Distribution volume ratios without blood sampling from graphical analysis of PET data. J. Cereb. Blood Flow Metab. 16 (5), 834 840.

Lopresti, B.J., Klunk, W.E., Mathis, C.A., Hoge, J.A., Ziolko, S.K., Lu, X., Meltzer, C.C., Schimmerl, K., Tsopelas, N.D., DeKosky, S.T., Price, J.C., 2005. Simplified quantification of Pittsburgh Compound B amyloid imaging PET studies: a comparative analysis. J. Nucl. Med. 46 (12), 1959 1972.

Mathis, C.A., Wang, Y., Holt, D.P., Huang, G.-F., Debnath, M.L., Klunk, W.E., 2003. Synthesis and evaluation of ^{11}C-labeled 6-substituted 2-arylbenzothiazoles as amyloid imaging agents. J. Med. Chem. 46 (13), 2740 2754.

Mishina, M., Ishiwata, K., Kimura, Y., Naganawa, M., Oda, K., Kobayashi, S., Katayama, Y., Ishii, K., 2007. Evaluation of distribution of adenosine A$_{2A}$ receptors in normal human brain measured with [^{11}C]TMSX PET. Synapse 61 (9), 778 784.

Naganawa, M., Kimura, Y., Ishii, K., Oda, K., Ishiwata, K., Maiani, A., 2005a. Extraction of a plasma time activity curve from dynamic brain PET images based on independent component analysis. IEEE Trans. Biomed. Eng. 52 (2), 201 210.

Naganawa, M., Kimura, Y., Nariai, T., Ishii, K., Oda, K., Manabe, Y., Chihara, K., Ishiwata, K., 2005b. Omission of serial arterial blood sampling in neuroreceptor imaging with independent component analysis. NeuroImage 26 (3), 885 890.

Naganawa, M., Kimura, Y., Ishii, K., Oda, K., Ishiwata, K., 2007a. Temporal and spatial blood information estimation using Bayesian ICA in dynamic cerebral positron emission tomography. Digit. Signal Process. 17 (5), 979 993.

Naganawa, M., Kimura, Y., Mishina, M., Manabe, Y., Chihara, K., Oda, K., Ishii, K., Ishiwata, K., 2007b. Quantification of adenosine A$_{2A}$ receptors in the human brain using [^{11}C]TMSX and positron emission tomography. Eur. J. Nucl. Med. Mol. Imaging 34 (5), 679 687.

Di Paola, R., Bazin, J.P., Aubry, F., Aurengo, A., Cavailloles, F., Herry, J.Y., Kalin, F., 1982. Handling of dynamic sequences in nuclear medicine. IEEE Trans. Nucl. Sci. NS-29 (4), 1310 1321.

Price, J.C., Klunk, W.E., Lopresti, B.J., Lu, X., Hoge, J.A., Ziolko, S.K., Holt, D.P., Meltzer, C.C., DeKosky, S.T., Mathis, C.A., 2005. Kinetic modeling of amyloid binding in humans using PET imaging and Pittsburgh Compound-B. J. Cereb. Blood Flow Metab. 25 (11), 1528 1547.

Wang, Z.J., Peng, Q., Liu, K.J.R., Szabo, Z., 2005. Model-based receptor quantization analysis for PET parametric imaging. 27th Annual International Conference of the IEEE Engineering in Medicine and Biology Society, pp. 5908 5911.

Watabe, H., Channing, M.A., Der, M.G., Adams, H.R., Jagoda, E., Herscovitch, P., Eckelman, W.C., Carson, R.E., 2000. Kinetic analysis of the 5-HT$_{2A}$ ligand [^{11}C]MDL 100.907 J. Cereb. Blood Flow Metab. 20, 899 909.

Wu, H.M., Hoh, C.K., Choi, Y., Schelbert, H.R., Hawkins, R.A., Phelps, M.E., Huang, S.C., 1995. Factor analysis for extraction of blood time activity curves in dynamic FDG-PET studies. J. Nucl. Med. 36 (9), 1714 1722.

Decreased cortical glucose metabolism in converters from CDR 0.5 to Alzheimer's disease in a community: the Osaki-Tajiri Project

Hiroshi Ishii,[1,2] Hiroyasu Ishikawa,[1,3] Kenichi Meguro,[1,3] Manabu Tashiro[4] and Satoshi Yamaguchi[1,3]

[1] Department of Geriatric Behavioral Neurology, Tohoku University Graduate School of Medicine, Sendai, Japan
[2] Kawasaki Kokoro Hospital, Kawasaki, Japan
[3] The Osaki-Tajiri SKIP Center, Osaki, Japan
[4] Division of Nuclear Medicine, Cyclotron Radioisotope Center, Tohoku University, Sendai, Japan

ABSTRACT

Background: Several follow-up [^{18}F]fluorodeoxy glucose (FDG)-positron emission tomography (PET) studies have been performed in patients with mild cognitive impairment, but none have examined subjects with a Clinical Dementia Rating (CDR) of 0.5. Therefore, we used FDG-PET to investigate whether baseline glucose metabolism (CMRglc) in CDR 0.5 converters to dementia showed changes consistent with early Alzheimer's disease (AD).

Methods: Based on our earlier study, which we refer to as Prevalence Study 1998, we were able to examine 14 CDR 0, 42 CDR 0.5, and 12 AD subjects with PET and follow these subjects for five years. Baseline neuropsychological and CMRglc values were compared among groups of CDR 0, CDR 0.5/converters, CDR 0.5/non-converters, and AD subjects.

Results: All CDR 0 subjects were reassessed as CDR 0 after the five-year period. For CDR 0.5 subjects, 20 had converted to AD and 22 remained as CDR 0.5. In cognitive tests, CDR 0.5/converters showed significantly deteriorated recent memory function compared with CDR 0.5/non-converters at the baseline evaluation. Most brain areas showed decreased CMRglc in AD patients. CDR 0.5/converters had a significantly lower baseline CMRglc in the right cingulate, left inferior parietal and left temporal gyrus compared with CDR 0.5/non-converters.

Conclusions: Our findings suggest that CDR 0.5/converters have a baseline metabolic decline in areas that might be specific to AD.

Key words: MCI, CDR 0.5, FDG, PET, Alzheimer's disease

Introduction

Early diagnosis of the borderline condition between healthy aging and dementia may be important for health policy planning for dementia prevention or early intervention, since some borderline cases are reported to be reversible (Larrieu et al., 2002). This condition is referred to as mild cognitive impairment (MCI) (Petersen et al., 1997) or Clinical Dementia Rating (CDR; Morris, 1993) 0.5, and the rate of progression to dementia is 8–20% per year. Impairment of cognitive functions such as recent memory and executive function (Chen et al., 2000) and a lower clinical observation score (Morris et al., 2001) are predictors of decline.

Hippocampal atrophy (Visser et al., 2002) shown by magnetic resonance imaging (MRI) is characteristic of the neurological background of CDR 0.5 subjects, particularly in association with early Alzheimer's disease (AD). Five major longitudinal studies of MCI have been performed using the baseline cerebral metabolic rate for glucose (CMRglc) determined by positron emission tomography (PET) with [^{18}F]fluoro-deoxyglucose (FDG) (Arnaiz et al., 2001; Chetelat et al., 2003; Drzezga et al., 2003; Mosconi et al., 2004; Fellgiebel et al., 2007). All these studies used clinic samples, with four using neuropsychological tests based on Petersen's MCI criteria (Petersen et al., 1997) and the fifth using Global Deterioration Scale (GDS)

Correspondence should be addressed to: Kenichi Meguro, MD, PhD, Department of Geriatric Behavioral Neurology, Tohoku University Graduate School of Medicine, 2-1, Seiryo-machi, Aoba-ku, Sendai 980-8575, Japan. Email: k-meg@umin.ac.jp. Received 19 May 2008; revision requested 28 Jul 2008; revised version received 17 Sep 2008; accepted 25 Sep 2008. First published online 1 December 2008.